Accurate boundary treatments for lattice Boltzmann simulations of electric fields and electro-kinetic applications

2013 J. Phys. A: Math. Theor. 46 475501

(http://iopscience.iop.org/1751-8121/46/47/475501)

J. Phys. A: Math. Theor. **46** (2013) 475501 (15pp) doi:10.1088/1751-8113/46/47/475501

Accurate boundary treatments for lattice Boltzmann simulations of electric fields and electro-kinetic applications

Othmane Oulaid[1], **Qing Chen**[1,2] **and Junfeng Zhang**[1,3]

[1] Bharti School of Engineering, Laurentian University, Sudbury, ON P3E 2C6, Canada
[2] School of Energy and Power Engineering, Nanjing University of Science and Technology, Jiangsu 210094, People's Republic of China

E-mail: jzhang@laurentian.ca.

Received 12 June 2013, in final form 10 October 2013
Published 11 November 2013
Online at stacks.iop.org/JPhysA/46/475501

Abstract
In this paper a novel boundary method is proposed for lattice Boltzmann simulations of electric potential fields with complex boundary shapes and conditions. A shifted boundary from the physical surface location is employed in simulations to achieve a better finite-difference approximation of the potential gradient at the physical surface. Simulations are presented to demonstrate the accuracy and capability of this method in dealing with complex surface situations. An example simulation of the electrical double layer and electro-osmotic flow around a three-dimensional spherical particle is also presented. These simulated results are compared with analytical predictions and are found to be in excellent agreement. This method could be useful for electro-kinetic and colloidal simulations with complex boundaries, and can also be readily extended to other phenomena and processes, such as heat transfer and convection-diffusion systems.

PACS numbers: 02.60.Cb, 47.11.−j, 47.57.jd, 47.61.Fg, 68.08.De

(Some figures may appear in colour only in the online journal)

1. Introduction

The lattice Boltzmann method (LBM) has been generally accepted as a useful simulation method for complex flows [1–3]. By recognizing the mathematical connection between the propagation-collision particulate dynamics in the lattice Boltzmann algorithm and the corresponding differential equations from the Chapman–Enskog analysis, LBM models have

[3] Author to whom any correspondence should be addressed.

also been developed for various phenomena and processes, including the convection-diffusion processes, heat transfer, shallow water flows, flows in porous media, electric field and magnetic field [2]. For example, He and Li [4] have proposed an LBM model for the electric potential field in electrochemical processes with ion transport considered. In combination with a multiple-component LBM model, this scheme has also been utilized to study the electrohydrodynamic drop deformation in an electric field [5]. More extensively, electro-kinetic flows in microchannels and even porous structures have been investigated by integrating various LBM models for fluid flows, electric fields, heat transfer and even convection-diffusion processes [6–8]. When compared with other more traditional numerical methods (for example, the finite-difference method) for solving partial differential equations, the LBM approach is advantageous in dealing with complex boundary geometries and could be potentially more efficient with advanced computational technologies, such as GPU (graphics processing unit) computing [2, 9–11].

As with other numerical methods, boundary conditions play crucial roles for the simulation validity and stability. However, unlike the tremendous efforts in developing accurate boundary treatments for the LBM models of fluid flows [12–15], boundary methods for the LBM models of electric field have not been addressed adequately. Typical electric field LBM simulations are performed in regular domains with flat boundaries aligned along the lattice grid lines. Several studies have considered rough surfaces [8, 16, 17]; however, the rough surfaces were actually modeled as flat, stair-like patches. In addition, most of the previous studies have only considered the Dirichlet BCs (with surface potential given), while Neumann (with surface charge given) and even Robin (with surface charge regulation relationship given) BCs are frequently encountered in electro-kinetic and colloidal systems [18].

In this paper, we extend an LBM boundary method for fluid flows [14] to simulations of electric fields with arbitrary boundary shapes. A novel scheme is also proposed to impose Neumann or Robin BCs of electric potential on curved surfaces by introducing a shifted boundary. Numerical simulations demonstrate that the boundary treatments have accurately represented the spatial geometry as well as the surface potential/charge conditions. Our simulations with different relaxation parameter values suggest that a larger relaxation parameter is preferable for a faster convergence and a better numerical stability. A three-dimensional (3D) example calculation is also performed to illustrate the application of our boundary method for electro-kinetics studies. This study could be useful for LBM simulations of electric fields in systems with complex surface geometry and surface conditions, including porous and particulate flows. The method proposed here can also be readily extended to other LBM formulations for electric fields (three dimension models, multi-relaxation-time models, etc) as well as other phenomena and processes (convection-diffusion processes, heat transfer, etc).

2. Method description

2.1. Lattice Boltzmann model for electric potential field

The electric field is governed by the well-known Poisson equation

$$\nabla^2 \psi = -\rho_e/\epsilon, \tag{1}$$

where ψ is the electric potential, ρ_e is the net electric charge density, and ϵ is the medium permittivity. Here, to solve this equation, we adopt an LBM algorithm originally proposed for the convection-diffusion processes for its good numerical accuracy [19]. The Poisson equation can be considered as a diffusion-convection equation at the steady state and with no flows.

A lattice distribution function f_i is introduced, and its evolution is described by the following lattice Boltzmann equation

$$f_i(\mathbf{x}+\mathbf{c}_i\triangle t, t+\triangle t) - f_i(\mathbf{x},t) = -\frac{f_i(\mathbf{x},t) - f_i^{\mathrm{eq}}(\mathbf{x},t)}{\tau} + \triangle t F_i + \frac{\triangle t^2}{2}\bar{D}_i F_i, \tag{2}$$

where $\mathbf{x}$ is the location, τ is a relaxation parameter, and $\triangle t$ is the simulation time step. F_i is related to the net charge term ρ_e/ϵ in equation (1) by

$$F_i = -\omega_i \alpha \rho_e/\epsilon, \tag{3}$$

and the operator $\bar{D}_i = \partial_t + \theta \mathbf{c}_i \cdot \nabla$, with $\theta \in [0,1]$ as a parameter for different difference schemes [19]. Both the minimum and maximum values of θ (0 and 1) have been tested with diffusion and convection-diffusion systems, and no significant influence on the solution accuracy is found [19]. In this work we set $\theta = 1$ for simplicity. For a D2Q9 (2D, 9 lattice velocities) lattice structure utilized in this work, the lattice velocities are

$$\mathbf{c}_0 = (0,0); \tag{4}$$

$$\mathbf{c}_i = [\cos(i-1)\pi/2, \sin(i-1)\pi/2]\triangle x/\triangle t, \; i = 1-4; \tag{5}$$

$$\mathbf{c}_i = [\cos(2i-9)\pi/4, \sin(2i-9)\pi/4]\triangle x/\triangle t, \; i = 5-8, \tag{6}$$

and the lattice weight factors are $\omega_0 = 4/9$, $\omega_{1-4} = 1/9$, and $\omega_{5-8} = 1/36$. $\triangle x$ is the lattice grid resolution. The parameter α in equation (3) is given by

$$\alpha = \frac{(2\tau - 1)\triangle x^2}{6\triangle t}. \tag{7}$$

The electric potential ψ can be calculated from the distribution functions by

$$\psi = \sum_i f_i \tag{8}$$

and the equilibrium distribution f_i^{eq} is related to the local potential value ψ via

$$f_i^{\mathrm{eq}} = \omega_i \psi. \tag{9}$$

Through a Chapman–Enskog analysis, the following differential equation can be derived [19]:

$$\frac{\partial \psi}{\partial t} = \alpha \nabla^2 \psi - \alpha \rho_e/\epsilon, \tag{10}$$

and the solution to the original Poisson equation (1) can be obtained at the steady state of the simulation when the partial differential term on the left-hand side approaches zero.

2.2. Boundary treatment for arbitrary surface geometry

Recently, Xiong and Zhang have modified the extrapolation method for boundary velocity by Guo *et al* [14] to study the momentum diffusion in uniform channel flows [20]. Here, we follow their modification and apply it to the electric field simulations. Consider a lattice link connecting a fluid node $\mathbf{x}_f$ and a solid node $\mathbf{x}_s$ and intersecting with the boundary at $\mathbf{x}_b$ (figure 1). The distribution function $f_i^+(\mathbf{x}_s, t)$, which is leaving the solid node $\mathbf{x}_s$ after collision in the $\mathbf{c}_i$ direction ($i = 8$ in figure 1) and will arrive at the fluid node $\mathbf{x}_f$ at next time step, can be expressed as [14]

$$f_i^+(\mathbf{x}_s) = f_i^{\mathrm{eq}}(\mathbf{x}_s) + \left(1 - \frac{1}{\tau}\right) f_i^{\mathrm{neq}}(\mathbf{x}_s), \tag{11}$$

where the equilibrium part is given by

$$f_i^{\mathrm{eq}}(\mathbf{x}_s) = \omega_i \psi(\mathbf{x}_s) \tag{12}$$

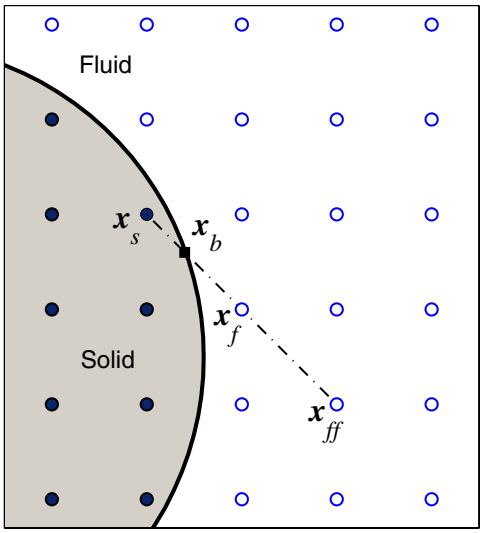

Figure 1. Boundary treatment for general surface geometry. A lattice link (dashed line) intersecting with the boundary (thick line) at $\mathbf{x}_b$ connects a fluid node $\mathbf{x}_f$ and a solid node $\mathbf{x}_s$. The next fluid node $\mathbf{x}_{ff}$ may be used if the first fluid node $\mathbf{x}_f$ is too close to the surface $\mathbf{x}_b$. See text for details.

and the non-equilibrium part f_i^{neq} will be discussed soon. Since the solid node $\mathbf{x}_s$ is outside of the fluid domain, the potential ψ and distribution functions at this position are in fact only fictitious values. We assume a linear variation of ψ along the lattice direction (dashed line in figure 1) and then the unknown $\psi(\mathbf{x}_s)$ is approximated as

$$\psi(\mathbf{x}_s) = \frac{1}{\triangle}\psi(\mathbf{x}_b) + \frac{\triangle - 1}{\triangle}\psi(\mathbf{x}_f),\ \triangle \geqslant 0.75; \tag{13}$$

$$\psi(\mathbf{x}_s) = \frac{2}{\triangle + 1}\psi(\mathbf{x}_b) + \frac{\triangle - 1}{\triangle + 1}\psi(\mathbf{x}_{ff}),\ \triangle < 0.75. \tag{14}$$

Here $\triangle = |\mathbf{x}_f - \mathbf{x}_b|/|\mathbf{x}_f - \mathbf{x}_s|$ and $\mathbf{x}_{ff}$ is the fluid node on the opposite of $\mathbf{x}_f$, i.e., $\mathbf{x}_{ff} = 2\mathbf{x}_f - \mathbf{x}_s$ (figure 1). Following the process of Guo *et al* [14], we estimate the unknown non-equilibrium distribution f_i^{neq} at the solid node $\mathbf{x}_s$ as:

$$f_i^{\text{neq}}(\mathbf{x}_s) = f_i^{\text{neq}}(\mathbf{x}_f),\ \triangle \geqslant 0.75; \tag{15}$$

$$f_i^{\text{neq}}(\mathbf{x}_s) = \triangle f_i^{\text{neq}}(\mathbf{x}_f) + (1 - \triangle) f_i^{\text{neq}}(\mathbf{x}_{ff}),\ \triangle < 0.75, \tag{16}$$

with $f_i^{\text{neq}}(\mathbf{x}) = f_i(\mathbf{x}) - f_i^{\text{eq}}(\mathbf{x})$ as the non-equilibrium part of the density distribution f_i. Through equations (11)–(15), once we have the surface potential $\psi(\mathbf{x}_b)$, we are able to estimate the incoming distributions $f_i^+(\mathbf{x}_s)$ across the boundary to the fluid domain, and the collision step (the right-hand side of equation (2)) at the boundary fluid node $\mathbf{x}_f$ can be performed.

2.3. Boundary treatment for potential gradient

The boundary method described above requires the surface potential value at $\mathbf{x}_b$. For Dirichlet BCs with surface potential available, the formulation is already complete. However, for Neumann and Robin BCs with the potential gradient on the surface involved, the surface potential is not explicitly specified and has to be obtained from the given BCs. A straightforward approach is to assume a forward finite-difference (FD) relationship from the boundary point

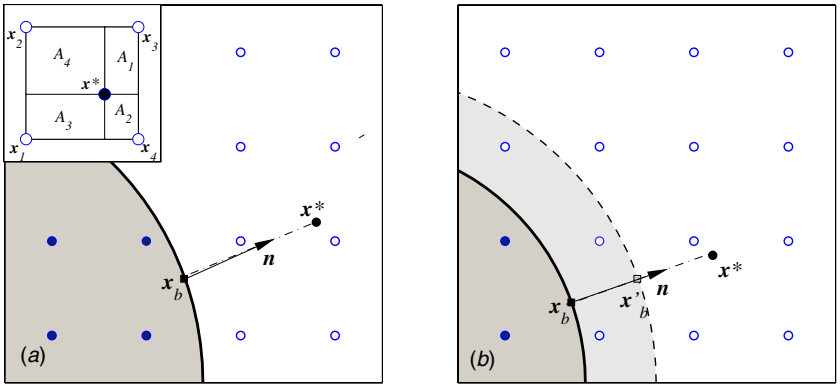

Figure 2. Boundary treatment for the potential gradient at a surface. (*a*) For the first-order FD approximation equation (17), the simulation considers the physical surface location (thick curve) and the potential value at point $\mathbf{x}^*$ is used to estimate the potential gradient at the boundary point $\mathbf{x}_b$. (*b*) For the second-order FD approximation equation (22), the simulation considers a shifted surface (thick curve) of $\delta/2$ from the physical surface location (thin dashed curve), and the potential value at point $\mathbf{x}^*$ is used to estimate the potential gradient at the boundary point $\mathbf{x}'_b$. In both cases, the point $\mathbf{x}^*$ locates at a δ-distance from the simulation surface (thick curve) in the normal direction $\mathbf{n}$. The inset in (*a*) illustrates the interpolation of potential value at $\mathbf{x}^*$ from the neighboring lattice nodes via equation (18).

$\mathbf{x}_b$ to a point in the fluid domain $\mathbf{x}^*$ of a distance δ in the normal direction $\mathbf{n}$ to the surface (figure 2(*a*)):

$$\left(\frac{\partial\psi}{\partial n}\right)(\mathbf{x}_b) \approx \frac{\psi(\mathbf{x}^*) - \psi(\mathbf{x}_b)}{\delta}, \tag{17}$$

and the potential at $\mathbf{x}^*$ can be estimated via an appropriate interpolation scheme, for example, for our current D2Q9 lattice structure,

$$\psi(\mathbf{x}^*) \approx \frac{\sum_{i=1}^{4} A_i \psi(\mathbf{x}_i)}{(\triangle x)^2}, \tag{18}$$

with $\mathbf{x}_i$ the four nearest lattice nodes and A_i the corresponding fractional areas in the lattice cell (see figure 2(*a*) inset). As a result, the boundary potential $\psi(\mathbf{x}_b)$ can be evaluated as

$$\psi(\mathbf{x}_b) \approx \psi(\mathbf{x}^*) - \delta\left(\frac{\partial\psi}{\partial n}\right)(\mathbf{x}_b) \tag{19}$$

for the Neumann BCs with $\partial\psi/\partial n$ available on the surface, and similarly

$$\psi(\mathbf{x}_b) \approx \frac{a\psi(\mathbf{x}^*) - c\delta}{a - b\delta} \tag{20}$$

for the mixed Robin BCs given by

$$a\frac{\partial\psi}{\partial n} + b\psi = c, \tag{21}$$

with a, b and c as prescribed constants or variables (for example, for heterogeneous surfaces or dynamic charge regulation processes).

The FD approximation in equation (17) is only of the first-order accuracy of δ [21]. To achieve a better accuracy, in general FD methods, a fictitious node on the solid side of the boundary $\mathbf{x}_b$ is introduced, and then the discrete FD relationship from the original differential equation is applied to $\mathbf{x}_b$ with its neighboring nodes involved [21]. This method

has a second-order accuracy of δ in estimating the boundary gradient; however, the algorithm is relatively complicated. Potential values at the locations in the tangential direction (both sides) are necessary, and it is difficult to be employed for general curved surfaces. Here, in the simulation, we propose to consider, instead of the real boundary location, a surface shifted by a distance $\delta/2$ from the real physical surface location into the solid side (figure 2(*b*)). The forward FD approximation in equation (17) now can be considered as a central FD approximation of the potential gradient at $\mathbf{x}'_b$ on the physical boundary with a second-order accuracy of δ:

$$\left(\frac{\partial\psi}{\partial n}\right)(\mathbf{x}'_b) \approx \frac{\psi(\mathbf{x}^*) - \psi(\mathbf{x}_b)}{\delta}, \tag{22}$$

since $\mathbf{x}'_b$ is the midpoint between $\mathbf{x}_b$ and $\mathbf{x}^*$. The right-hand side terms of equations (17) and (22) appear identical, and the linear slope between points $\mathbf{x}^*$ and $\mathbf{x}_b$ is both adopted as an approximation of the potential gradient on the surface. However, the linear slope in equation (17) is considered as the gradient at the interval end $\mathbf{x}_b$ (i.e., the forward FD scheme), while the slope in equation (22) is considered as the gradient at the center of the interval $\mathbf{x}'_b = (\mathbf{x}_b + \mathbf{x}^*)/2$ (i.e., the central FD scheme). By shifting the physical surface from $\mathbf{x}'_b$ into the solid domain by $\delta/2$ to the computational surface $\mathbf{x}_b$, now we have a better estimation of the potential gradient on the physical boundary location. The corresponding expression for $\psi(\mathbf{x}_b)$ for the Neumann BC is almost identical to that in equation (19), i.e.,

$$\psi(\mathbf{x}_b) \approx \psi(\mathbf{x}^*) - \delta\left(\frac{\partial\psi}{\partial n}\right)(\mathbf{x}'_b); \tag{23}$$

however, here $\mathbf{x}_b$ is on the shifted boundary and $(\partial\psi/\partial n)(\mathbf{x}'_b)$ is the potential gradient given at the physical boundary $\mathbf{x}'_b$. For a mixed Robin BC, the potential value at the physical boundary $\mathbf{x}'_b$ is also needed, and we assume it as the mean value of those at points $\mathbf{x}_b$ and $\mathbf{x}'_b$, since $\mathbf{x}_b$ is the midpoint between them:

$$\psi(\mathbf{x}'_b) \approx \frac{\psi(\mathbf{x}^*) + \psi(\mathbf{x}_b)}{2}. \tag{24}$$

Substituting equations (23) and (24) in the Robin BC equation (21) and solving $\psi(\mathbf{x}_b)$ yields

$$\psi(\mathbf{x}_b) \approx \frac{(2a + b\delta)\psi(\mathbf{x}^*) - 2c\delta}{2a - b\delta}. \tag{25}$$

3. Validation and demonstration simulations

3.1. Electric potential distributions between parallel plates

First, we consider a very simple system: two parallel plates with constant surface potentials. The plates are placed in a 20×5 domain along the y-direction. The centerline locates at $x = 10.5$, and the surface potentials are $\psi_1 = 1$ and $\psi_2 = 2$ at the left and right walls, respectively. Periodic BCs are applied at the top and bottom domain boundaries. Here, we consider no net charge between the plates (i.e., $\rho_e = 0$), and the Poisson equation (1) reduces to a Laplace equation for the electric potential ψ:

$$\nabla^2\psi = 0. \tag{26}$$

The analytical solution of this system is

$$\psi(x) = \psi_1 + \frac{\psi_2 - \psi_1}{x_2 - x_1}(x - x_1), \tag{27}$$

where x_1 and x_2 are the left and right wall locations, respectively.

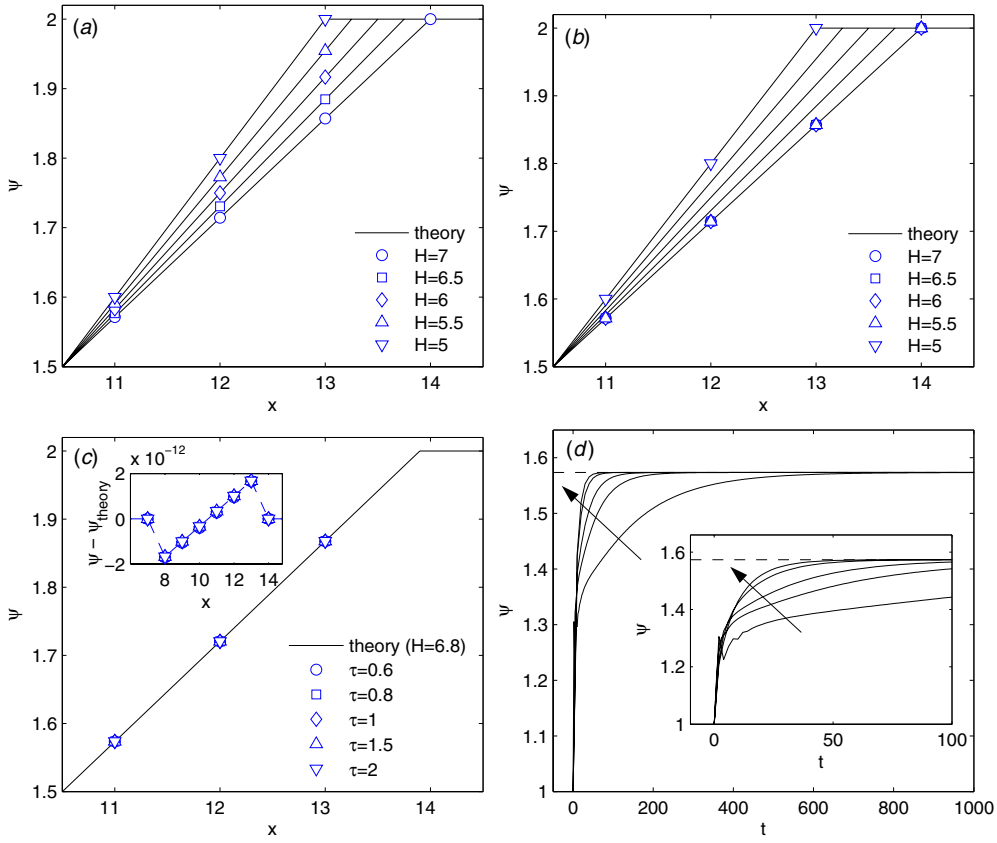

Figure 3. Electric potential distributions between two parallel plates with different separations calculated from our boundary treatment (*a*) and the method in [16] (*b*). The potential results for a separation of 6.8 with different relaxation parameter values are also presented in (*c*) and the inset there shows the differences between the simulated and analytical values. In these graphs, the symbols are from LBM simulations, and straight lines are from the analytical solution. Since the profiles are symmetric about the point of $x = 10.5$ and $\psi = (\psi_1 + \psi_2)/2 = 1.5$, only the right-top half-parts of the profiles are displayed for clarity. The converging processes at location $x = 11$ using different τ values from $\tau = 0.6, 0.8, 1, 1.5$ to 2.0 (in the arrow direction) are displayed in (*d*) and its inset shows more details in the early simulation period. The dashed line indicates the theoretical value $\psi = 1.5735$ at $x = 11$.

In our simulations, different plate separations $H = x_2 - x_1$ have been considered with $H = 5, 5, 5, 6, 6.5$ and 7. The relaxation parameter τ is set to 1 in all simulations in this study, unless specified otherwise. Simulation results from our method are presented in figure 3(*a*) as symbols, with the theoretical solutions from equation (27) displayed as lines. Clearly, excellent agreement can be observed there for all separations. For comparison, figure 3(*b*) displays the simulation results for the same systems with a boundary method utilized in previous studies for rough surfaces [16]. It is not surprising to see that method is not sensitive to the boundary location change, since the accurate surface position is not considered in the boundary formulations there [16]. For separations $H = 5.5$, 6, 6.5 and 7, the left and right walls locate, respectively, at $(x_1, x_2) = (7.75, 13.25)$, $(7.5, 13.5)$, $(7.25, 13.75)$ and $(7, 14)$. In these cases, the left wall is between 7 (solid node) and 8 (fluid node), while the right wall

is between 13 (fluid node) and 14 (solid node). The boundary method in [16] cannot tell the exact boundary location and it always assumes the first solid node along the boundary lattice link as the surface position. As a result, the left and right walls in these cases with different separations are all assumed as at $(x_1, x_2) = (7, 14)$. Clearly, this is only true for the case with $H = 7$. For the case with separation $H = 5$, the left wall locates at $x_1 = 8$ and right wall is at $x_2 = 13$. They are exactly at the solid node locations, and the method in [16] yields correct results again.

For the LBM model for flows with a single relaxation parameter, it has been observed that the relaxation parameter τ can induce artificial slip over boundaries. Here we examine the τ-effect on the calculated electric field, and the simulation results of a separation of $H = 6.8$ with $\tau = 0.6, 0.8, 1, 1.5$ and 2 are displayed in figure 3(*c*) with different symbols. We find that the results are exactly identical to each other and the symbols overlap, all agreeing excellently with the analytical prediction. This is even more evident by looking at the differences between the simulated and analytical potential distributions in the inset of figure 3(*c*). Here, symbols with different shapes have been utilized for different τ values; however, they completely overlap on top of each other, indicating that τ has no influence on the simulated potential field. The tiny difference values ($\sim 10^{-12}$) are mainly from the inevitable computer round-off errors. However, the relaxation parameter τ indeed participates in the computation in equation (2) and it is involved in the governing equation equation (10) via equation (7). According to equation (10), the parameter α, and therefore the relaxation parameter τ, is related to the temporal potential variation. When using such an LBM method to solve the electric potential field, we are only interested in the solution at the steady state when $\partial\psi/\partial t = 0$. We then look at the time evolution of the potential value at a particular position $x = 11$ for the separation $H = 6.8$ (left wall $x_1 = 7.1$; right wall $x_2 = 13.9$). The simulations start with an initial potential distribution as $\psi = 1$. Figure 3(*d*) shows how the potential value at $x = 11$ approaches the theoretical value 1.5735 (dashed line) as simulations process, with the inset there displaying the early simulation period. It take a much longer simulation time for the simulation with a low τ value to reach the steady state than that with a higher τ value, and even numerical oscillations could occur at very low τ values. The faster converging speed associated with a higher τ value is also consistent to equations (10) and (7): a higher τ value yields a larger α, which in turn implies a faster change in ψ. The results in figure 3(*d*) suggest that a higher τ value is preferable in simulations for fast convergence speed and good numerical stability.

3.2. Electric potential between coaxial circular surfaces

Next, to examine the performance of our method for more complex boundary shapes and conditions, we consider the electric field between two coaxial circular surfaces with inner and outer radii R_1 and R_2, respectively. With no net charge, the general solution to the Laplace equation (26) is given as

$$\psi(r) = C_1 \ln r + C_2, \tag{28}$$

where the constants C_1 and C_2 can be determined by BCs on the surfaces. Three boundary situations are investigated in this section.

(1) Case DD: Dirichlet BCs on both surfaces with $\psi(R_1) = \psi_1$ and $\psi(R_2) = \psi_2$.
(2) Case DN: Dirichlet BC on the inner surface with $\psi(R_1) = \psi_1$, and Neumann BC on the outer surface with $\frac{\partial\psi}{\partial n}(R_2) = \psi_2'$.
(3) Case RD: Robin BC on the inner surface as given in equation (21), and Dirichlet BC on the outer surface with $\psi(R_2) = \psi_2$.

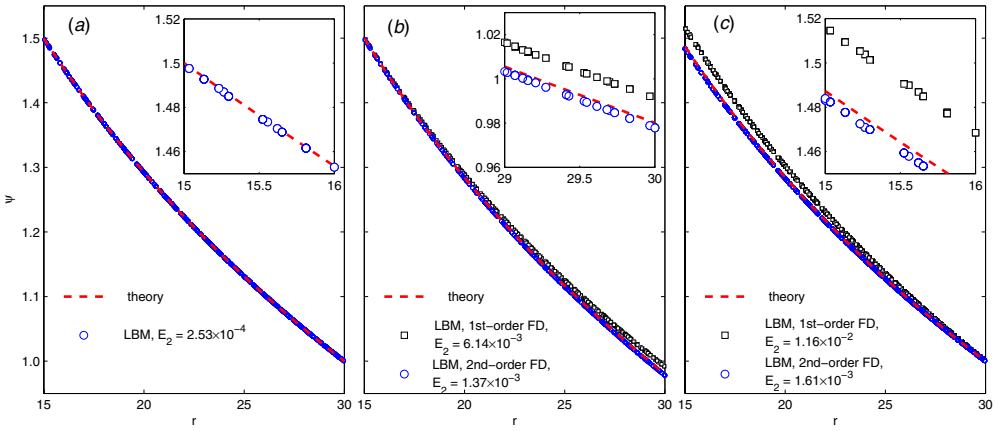

Figure 4. Electric potential distributions between two coaxial circular surfaces of $R_1 = 15$ and $R_2 = 30$ with different boundary situations: (*a*) case DD, (*b*) case DN and (*c*) case RD. The symbols are LBM simulated data, and the red dashed curves are the theoretical solutions. In (*b*) and (*c*), the black squares are results obtained by using the first-order FD scheme, and the blue circles are from the second-order FD approximation. The relative error for each case is also provided in the legend text. More details can be seen in the inset graphs.

The corresponding exact solutions for these cases are:

$$\psi(r) = \psi_1 + (\psi_2 - \psi_1)\frac{\ln(r/R_1)}{\ln(R_2/R_1)} \quad \text{for case DD,} \tag{29}$$

$$\psi(r) = \psi_1 + R_2\psi_2' \ln(r/R_1) \quad \text{for case DN,} \tag{30}$$

and

$$\psi(r) = \psi_2 + \frac{b\psi_2 - c}{b\ln(R_2/R_1) - a/R_1}\ln(r/R_2) \quad \text{for case RD.} \tag{31}$$

In our first group of simulations, we set $R_1 = 15$ and $R_2 = 30$ for all the three cases. The BC parameters are: $\psi_1 = 1.5$ and $\psi_2 = 1$ for case DD; $\psi_1 = 1.5$ and $\psi_2' = 0.025$ for case DN; and $a = 18$, $b = 0.5$, $c = -0.1$ in equation (21) on the inner surface and $\psi_2 = 1$ on the outer surface for case RD. The domain size is 101×101 and the surfaces are put at the center of the domain. For cases DN and RD, both the first-order and second-order FD schemes for the boundary gradient have been considered with $\delta = 1.5$, and the effect of different δ values will be examined later. The relative error is defined as

$$E_2 = \left\{\frac{\sum[\psi_{LBM}(\mathbf{x}) - \psi_{\text{theory}}(\mathbf{x})]^2}{\sum[\psi_{\text{theory}}(\mathbf{x})]^2}\right\}^{1/2} \tag{32}$$

to quantify the simulation deviation from the analytical solution. Here, $\psi_{LBM}(\mathbf{x})$ and $\psi_{\text{theory}}(\mathbf{x})$ are, respectively, the calculated and theoretical potential values at the lattice node $\mathbf{x}$, and both summations are taken over all lattice nodes between the two circular surfaces. Simulation results for these systems are plotted in figure 4 with relative errors also provided in the graph legends. First of all, we see the simulation data symbols for each case exhibit a clear trend instead of scatters. This indicates that our boundary method can produce a good isotropy in different lattice directions and boundary orientations, which is a fundamental concern in the LBM methods. In general, the results for case DD and cases DN and RD using the second-order FD schemes (blue circles) agree well with theory (red dashed lines). The lowest relative error

is found for case DD with the Dirichlet BCs on both surfaces, where no FD approximation is involved. The relative error increases when an FD scheme is employed, and it is smaller when the second-order scheme is adopted (blue circles versus black squares). It is also evident in figures 4(*b*) and (*c*) (see the inset graphs) that the major deviation from analytical solution occurs near the surface where the potential gradient is estimated by the FD schemes. In addition, for the same FD scheme, the relative error in case RD is slightly larger than that in case DN, since the potential gradient approximation is conducted near the inner surface with a higher curvature (less flat) in case RD.

In the above simulations, the value of δ is set as 1.5. Intuitively, one will anticipate a better numerical accuracy with a smaller δ distance, over which the FD approximation is performed. However, too small a δ value may result in an interpolation point $\mathbf{x}^*$ too close to the boundary with some of its neighboring lattice nodes $\mathbf{x}_i$ even in the solid domain (see figure 2(*a*) inset). This situation should be avoided since it will damage the correct interpolation of $\psi(\mathbf{x}^*)$ via equation (18). For flat surfaces, the low limit of δ is $\sqrt{2}\triangle x$, the diagonal length of the square lattice cell. For curved surfaces, this limit value usually would be larger, depending on the particular boundary shape and location. For our simulations here, $\delta = 1.5$ is good enough to avoid any solid nodes being involved in the interpolation. Nevertheless, it would be interesting to examine the δ effect on the simulation results. Here, in addition to the results from $\delta = 1.5$ in figures 4(*b*) and (*c*), we re-do these simulations with $\delta = 2.0$ and 2.5, for both the cases DN and RD and using both the first-order and second-order FD approximations. These results are presented in figure 5 with the relative errors provided in the legend texts. When the first-order FD approximation is employed, we indeed see that the numerical error increases with δ, approximately linearly (figures 5(*a*) and (*c*)). This confirms our initial intuition and implies that the relatively larger errors are mainly from the less accurate FD evaluations. On the other hand, when the second-order FD approximation is adopted, the numerical error is much less sensitive to the δ change. It actually decreases slightly with the increase in δ for the DN case (figure 5(*b*)), and the $E_2 \sim \delta$ relationship is even not monotonic for the case RD (figure 5(*d*)). One fact we should be aware of is that, with the second-order FD scheme, the physical boundary location has shifted by a $\delta/2$ distance toward the solid domain (figure 2(*b*)). When a larger δ is employed, the boundary treatment is implemented at a location farther away from the physical boundary, and the regular LBM calculation is less disturbed near the physical boundary. This is helpful to reduce the numerical errors calculated over the physical domain only up to the physical boundary. The insensitive response of relative errors might be a compromise between the counter-effects from the decreasing FD accuracy and the increasing simulation accuracy as δ increases. Based on these simulations, we will only consider the second-order FD scheme with $\delta = 1.5$ in the next simulations.

Furthermore, the dependence of relative error on the grid resolution $\triangle x$ is also examined for cases DD and DN by varying the outer radius R_2 with the radius ratio $R_1/R_2 = 1/2$ kept constant. For the case DD, the surface potentials do not change with the system size (i.e., $\psi_1 = 1.5$ and $\psi_2 = 1$). For cases DN, we hold the surface potential on the inner surface constant with $\psi_1 = 1.5$ but vary the potential gradient on the outer surface according to $\psi_2' = 0.025R_2/30$, such that the resulting surface potential on the outer surface does not change with the system size. The relative error changes with the outer radius R_2 are plotted in figure 6 in logarithmic scales. For the same size, the relative error for the case DN is always larger than that for the case DD. When the radii change, approximately linear trends are observed, and the negative slopes from linear fittings are 1.986 and 1.352, respectively, for the cases DD and DN. For the case DD with surface potential directly available and no further FD schemes involved, our boundary method has preserved well the basic second-order accuracy of the LBM algorithm [19]. The larger errors and lower accuracy order for the case DN are due

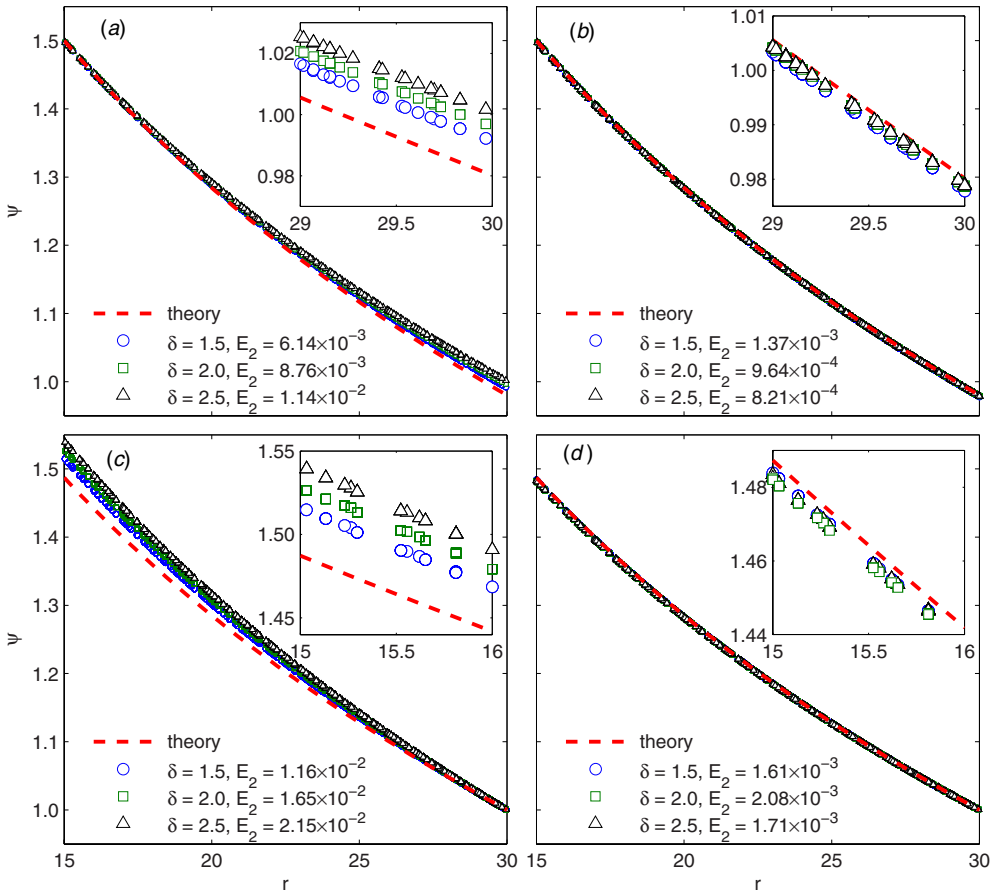

Figure 5. Effect of the FD distance δ on simulation accuracy for cases DN (*a*) and (*b*) and RD (*c*) and (*d*) with the first-order (*a*) and (*c*) and second-order (*b*) and (*d*) FD schemes. The symbols are LBM simulated data (blue circles for $\delta = 1.5$, green squares for $\delta = 2.0$, and black triangles for $\delta = 2.5$), and the red dashed curves are the theoretical solutions. The relative error for each case is also provided in the legend text. More details can be seen in the inset graphs.

to the necessary FD approximation on the outer surface via equation (22). It should be noted that although the FD scheme equation (22) has a second-order accuracy of the FD length δ, the boundary potential value required in the LBM calculation is still an approximation from the given potential gradient at boundary. This inaccuracy in the input boundary value will certainly downgrade the overall simulation accuracy, both in error magnitude and accuracy order. As shown in a recent study, the overall LBM simulation accuracy is a complex phenomenon and several factors (including the LBM algorithm, boundary conditions, systems simulated, and even the relative error definition) play roles [22]. Similar reduced accuracy has also been reported in previous studies, for example, when combining the LBM method for flows with the FD method for the Nernst–Planck and Poisson equations [23].

3.3. Example application in electro-osmotic flows

So far our simulations have not considered the net charge density term in the Poisson equation, and the system geometry is relatively simple. Finally, as an example to illustrate the usefulness

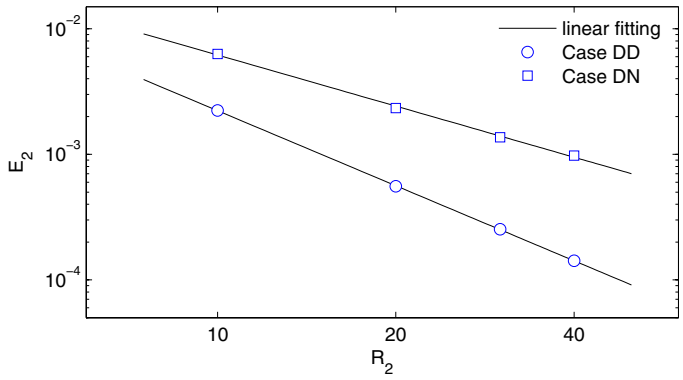

Figure 6. Relative errors between the simulated and theoretical potential distributions for cases DD (circles) and DN (squares) with different outer radius R_2. Linear fittings in this logarithmic graph for the symbols are also displayed as straight lines.

of our model in electro-kinetic microfluidics, we apply our method to simulate the electric potential distribution around a charged spherical particle immersed in an electrolyte solution. The particle has a radius of R and a constant potential ψ_0 on the surface. Near the charged surfaces, ions in the electrolyte solution will be redistributed and the electrical double layer (EDL) will be established. The ion charge density can be related to the local potential via the Boltzmann distribution,

$$\rho_i = \rho_i^0 \, \mathrm{e}^{-z_i e\psi/k_B T} \tag{33}$$

and the Poisson equation is then re-written to the classical Poisson–Boltzmann equation [18]

$$\nabla^2\psi = \frac{\sum_i z_i e \rho_i}{\epsilon}. \tag{34}$$

Here ρ_i is the density of ion i, of which the valency is z_i and the bulk density with no electric potential is ρ_i^0. e is the electron charge, k_B is the Boltzmann constant and T is the absolute temperature. For surfaces with low surface potentials, the Debye–Huckel approximation [18] can be applied and the Poisson–Boltzmann equation can be linearized to

$$\nabla^2\psi = \kappa^2\psi, \tag{35}$$

where

$$\kappa = \sqrt{\frac{\sum_i z_i^2 e^2 \rho_i^0}{\epsilon k_B T}} \tag{36}$$

and its reciprocal κ^{-1}, the so-called Debye length, is usually used as a measure of the EDL thickness. The solution of this linearized Poisson–Boltzmann equation around a spherical particle with thin EDL layers (i.e., $\kappa R \gg 1$) is given as

$$\psi(r) = \psi_0 \frac{R}{r} \, \mathrm{e}^{-\kappa(r-R)}, \tag{37}$$

where r is the distance to the sphere center. We use $\psi_0 = 1$ and $\kappa = 0.2$ in our simulation. The particle has a radius of $R = 30$, and its center (x_c, y_c, z_c) locates at the center of the $101\times101\times101$ cubic domain. Periodic boundary conditions are applied in all the three directions, and hence the simulated system actually represents a cubic array of spheres uniformly distributed in space, with a center-to-center distance of 101 in each direction.

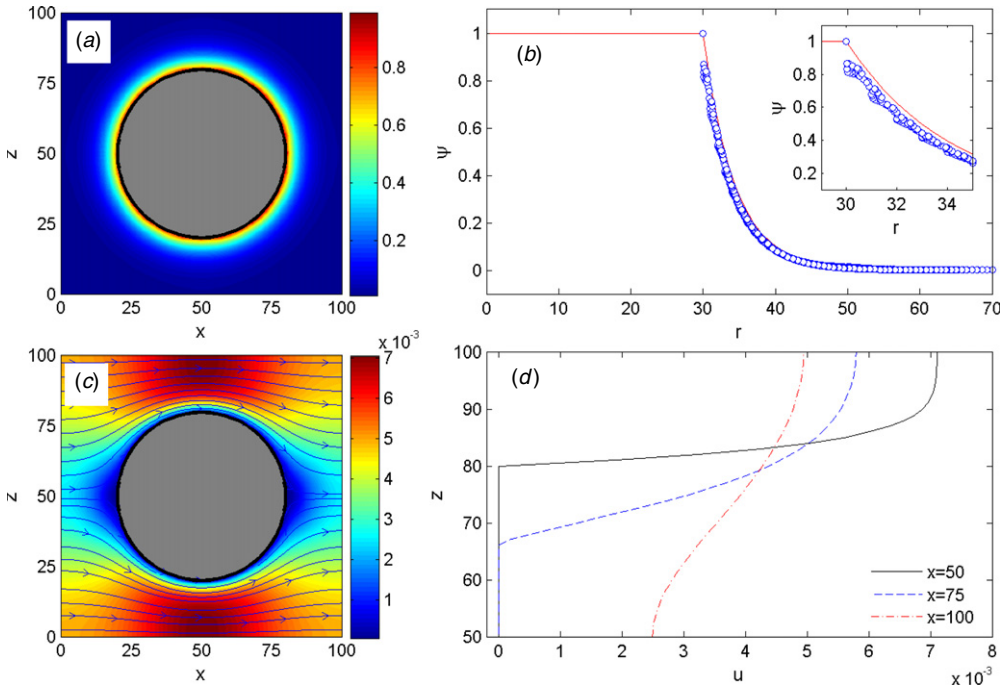

Figure 7. The electric potential distribution (*a*) and (*b*) and electro-osmotic flow (*c*) and (*d*) around the spherical particle in the $y = y_c$ plane. The analytical solution of electric potential (red curve) is compared to that from our LBM simulation (blue circles) in (*b*), and its inset displays the potential deviations near the particle surface. See text for detailed discussions.

The algorithm and boundary method described in previous sections have also been extended to the D3Q19 (three-dimensional and 19-velocity) lattice model to simulate this 3D system. The calculated potential distribution at the $y = y_c$ plane is presented in figure 7(*a*). For a more quantitative examination, in figure 7(*b*), we also plot the electrical potential ψ as a function of the distance r to the particle center. The blue circles are from our LBM calculation and the red curve is the analytical solution according to equation (37). Good agreement can be observed between them, and the few deviations near the particle surface are due to the large potential gradient as well as the particular assumption of thin EDL $\kappa R \gg 1$ ($\kappa R = 6$ in our system) in the theoretical solution equation (37). The distribution appears circularly symmetric in figure 7(*a*), and this is confirmed by the fact that all the simulated $\psi \sim r$ data points fall approximately on a single curve in figure 7(*b*). Again this shows that the system isotropy (since the EDL thickness is much smaller than the gap distance between surfaces) has been well preserved.

When an external electric field is applied, an electric force $\mathbf{F}_e$ will be generated in the electrolyte solution near the surface due to the non-zero net charge in that region, and this electrostatic force can thus induce fluid flows along the electric field direction. This phenomenon is called the electro-osmosis and such flows are called the electro-osmotic flows. In addition to the Poisson–Boltzmann equation for the electric field, the continuity equation

$$\frac{\partial \rho}{\partial t} + \nabla \cdot (\rho \mathbf{u}) = 0 \tag{38}$$

and Navier–Stokes equation with the electric force $\mathbf{F}_e$ as a forcing term

$$\frac{\partial \mathbf{u}}{\partial t} + (\mathbf{u} \cdot \nabla)\mathbf{u} = -\frac{1}{\rho}\nabla P + \frac{\mu}{\rho}\nabla^2 \mathbf{u} + \frac{\mathbf{F}_e}{\rho} \tag{39}$$

for fluid mechanics also need to be solved. Here $\mathbf{u}$ is the flow velocity, ρ is the fluid density, P is the pressure and μ is the fluid viscosity. Here the classic single-relaxation-time (SRT) LBM model with the improved bounce-back boundary method for flow fields [15] has been utilized. To simulate the electro-osmotic flow through the 3D sphere array studied here, we calculate the net charge density ρ_e from the electric potential field ψ obtained in our above calculation according to the Debye–Huckel approximation $\rho_e = -\epsilon\kappa^2\psi$. The electric force on fluid F_e can be calculated from ρ_e by multiplying it with the applied electric field strength E_0, i.e., $F_e = E_0\rho_e = -E_0\epsilon\kappa^2\psi$. The resultant electric force is then implemented in the LBM flow simulation to drive the fluid flow passing over the sphere particle. In this study, we have $E_0\epsilon = -0.01$, and the electric field E_0 is considered in the x-direction.

Figure 7(*c*) displays the electro-osmotic flow streamlines around the particle in the $y = y_c$ plane, and the background color indicates the velocity magnitude (red for large and blue for small magnitudes). The flow pattern is symmetric about both $x = x_c$ and $z = z_c$ due to the symmetric system geometry and the creeping electro-osmotic flow. The no-slip boundary condition on the circular particle surface has been well preserved as indicated by the flow pattern and the dark blue color near the surface. Also, the streamwise velocity component u in the x-direction of this flow at $x = 50$ (particle center), 75 and 100 (right boundary) are plotted in figure 7(*d*). Only the upper half ($z > z_c = 50$) is shown for these symmetric curves. At $x = 50$ (black solid line), the velocity increases from 0 at the surface to a plateau value near the top boundary. This is similar to the typical plug-like velocity profile of electro-osmotic flows in straight channels, since the electric force only exists in the thin EDL near the surface. Away from this particular location, the cross-sectional area for the flow passage increases, and therefore the flow velocity decreases due to the mass conservation. This simulation demonstrates the potential usefulness of our method for electro-kinetic flows in porous and particulate systems.

4. Summary

We have proposed to extend the extrapolation boundary method for LBM flow simulations to electric field simulations, and a novel, accurate method to approximate the potential gradient at surfaces with Neumann and Robin BCs by using a shifted boundary. Simulations have also been performed to examine our boundary methods in terms of spatial accuracy, ability to deal with various boundary situations, relaxation parameter effect and the accuracy-resolution relationship. Although the relaxation parameter has no impact on final potential solution at the steady state, a larger relaxation parameter (e.g., $\tau = 2$) provides a faster convergence and a better numerical stability. A 3D example simulation of the EDL structure near charged surfaces in electrolyte solutions and the electro-osmotic flow induced by an external electric field has also been presented. The sphere array system simulated here can be considered as a representative of particulate and porous flow systems, and it illustrates the potential usefulness of our boundary model in such applications. Comparisons with theoretical predictions show excellent agreement for all simulations, and our methods therefore could be useful for future electro-kinetic simulations with complex boundary geometries (rough surfaces, porous materials, colloid suspensions, etc) and/or various BC situations (constant-potential, constant-charge, dynamic charge regulation, heterogeneous surfaces, etc).

Although all method descriptions and most simulations here are for a SRT LBM scheme with the simple D2Q9 lattice structure, there are no technical difficulties in extending them

to other LBM algorithms (for example, multiple-relaxation-parameter models) and lattice structures. Furthermore, since the LBM simulation here is actually solving a convection-diffusion equation, the boundary treatments presented in this work can also be applied to LBM simulations for other processes and phenomena that can be described by similar differential equations, including heat transfer and convection-diffusion processes.

Acknowledgments

This work was supported by the Natural Science and Engineering Research Council of Canada (NSERC) and the Laurentian University Research Fund (LURF). QC acknowledges the visiting studentship from Nanjing University of Science and Technology for his study in Laurentian University. This work was made possible by the facilities of Westgrid (www.westgrid.ca) and SHARCNet (the Shared Hierarchical Academic Research Computing Network, www.sharcnet.ca).

References

[1] Succi S 2001 *The Lattice Boltzmann Equation* (Oxford: Oxford University Press)
[2] Zhang J 2011 *Microfluidics Nanofluidics* **10** 1
[3] Aidun C and Clausen J 2010 *Annu. Rev. Fluid Mech.* **42** 439
[4] He X and Li N 2000 *Comput. Phys. Commun.* **129** 158
[5] Zhang J and Kwok D Y 2005 *J. Comput. Phys.* **206** 150
[6] Guo Z, Zhao T and Shi Y 2005 *J. Chem. Phys.* **122** 144907
[7] Fu X, Li B, Zhang J, Tian F and Kwok D Y 2007 *Int. J. Mod. Phys.* C **18** 693
[8] Wang M, Wang J and Chen S 2007 *J. Comput. Phys.* **226** 836
[9] Huber C, Chopard B and Manga M 2010 *J. Comput. Phys.* **229** 7956
[10] Kang Q, Lichtner P C and Zhang D 2007 *Water Resour. Res.* **43** W12S14
[11] Tubbs K R and Tsai F T-C 2011 *Int. J. Numer. Methods Eng.* **86** 316
[12] Ladd A 1994 *J. Fluid Mech.* **211** 285
[13] Mei R, Luo L and Shyy W 1999 *J. Comput. Phys.* **155** 307
[14] Guo Z, Zheng C and Shi B 2002 *Phys. Fluids* **14** 2007
[15] Yin X and Zhang J 2012 *J. Comput. Phys.* **231** 4295
[16] Wang M and Kang Q 2009 *Anal. Chem.* **81** 2953
[17] Tang G, He Y and Tao W 2010 *J. Appl. Phys.* **107** 104906
[18] Israelachvili J 1991 *Intermolecular and Surface Forces* 2nd edn (San Diego, CA: Academic)
[19] Shi B, Deng B, R Du and Chen X 2008 *Comput. Math. Appl.* **55** 1568
[20] Xiong W and Zhang J 2011 *Comput. Math. Appl.* **61** 3453
[21] Golub G H and Ortega J M 1992 *Scientific Computing and Differential Equations: An Introduction to Numerical Methods* (London: Academic)
[22] Chen Q, Zhang X and Zhang J 2013 *Phys. Rev.* E **88** 033304
[23] Hlushkou D, Kandhai D and Tallarek U 2004 *Int. J. Numer. Methods Fluids* **46** 507